Supplemental Materials

Achromatic On-Chip Focusing of Graphene Plasmons for Spatial Inversions of Broadband Digital Optical Signals

Zhiyong Wu[1,2] and Zhengji Xu[1,2*]

[1]School of Microelectronics Science and Technology, Sun Yat-sen University, Zhuhai 519082, China;

[2]Guangdong Provincial Key Laboratory of Optoelectronic Information Processing Chips and Systems, Sun Yat-sen University, Zhuhai 519082, China.

[*]Corresponding author: xuzhj27@mail.sysu.edu.cn

Section 1: Dispersion equations of the AGPPs supported by the GIWAL in a single unit cell

To understand the design principle of the graded index waveguide array lens (GIWAL), we need to determine the effective refractive index of each unit cell in the GIWAL for the propagation of the AGPPs. For this purpose, we first theoretically analyze mode properties of the AGPPs supported by the GIWAL in each unit cell by solving the corresponding dispersion equation. Figure S1a shows an enlarged unit cell structure of the GIWAL. According to the idea of the effective index method,[45-47] this unit cell structure is divided into two parts: regions I and II (Figure S1a). Treating the widths of both regions I and II as infinite along the *x*-direction, we first calculate the effective wave-vector of the AGPPs propagating along the *z*-direction in each region.

Both regions I and II correspond to three-medium slab waveguides with a surface conductivity, as shown in Figure S1b. Since the AGPPs are transverse magnetic (TM) modes with magnetic field component mainly along the *x*-axis, the magnetic field component of the AGPPs propagating along the *z*-direction can be expressed as:

$$H_x(x,y,z,t)=\begin{cases} H_{1x}=Ae^{-k_1(y-\frac{d}{2})}e^{-i(\omega t-qz)} & d/2<y \\ H_{2x}=[Be^{k_2(y+\frac{d}{2})}+Ce^{-k_2(y+\frac{d}{2})}]e^{-i(\omega t-qz)} & -d/2<y<d/2, \\ H_{3x}=De^{k_3(y+\frac{d}{2})}e^{-i(\omega t-qz)} & y<-d/2 \end{cases} \quad \text{(A1)}$$

where $k_j^2 = q^2 - \varepsilon_j k_0^2$ (j = 1, 2, or 3), ε_j is the relative permittivity of the corresponding medium in Figure S1b, ω is the angular frequency of the incident light, and d is the thickness of the intermediate medium. q and k_0 are the effective wave-vector of the TM wave propagating along the *z*-direction and the wavenumber of the incident light in vacuum, respectively. A, B, C, and D are the four pending mode coefficients.

According to Maxwell's equations and the expression of H_x, the electric field component of the TM wave along the *z*-axis can be further solved as:

$$E_z(x,y,z,t)=\begin{cases} E_{1z}=-\dfrac{k_1}{i\omega\varepsilon_0\varepsilon_1}Ae^{-k_1(y-\frac{d}{2})}e^{-i(\omega t-qz)} & d/2<y \\ E_{2z}=\dfrac{k_2}{i\omega\varepsilon_0\varepsilon_2}[Be^{k_2(y+\frac{d}{2})}-Ce^{-k_2(y+\frac{d}{2})}]e^{-i(\omega t-qz)} & -d/2<y<d/2, \\ E_{3z}=\dfrac{k_3}{i\omega\varepsilon_0\varepsilon_3}De^{k_3(y+\frac{d}{2})}e^{-i(\omega t-qz)} & y<-d/2 \end{cases} \quad \text{(A2)}$$

where ε_0 is the permittivity in vacuum. Since the surface conductivity σ_g induces a surface current at *y*

= $d/2$, the boundary conditions satisfied by the TM mode in the waveguide become:

$$\begin{cases} E_{1z}\big|_{y=d/2} = E_{2z}\big|_{y=d/2} \\ H_{2x}\big|_{y=d/2} - H_{1x}\big|_{y=d/2} = \sigma_g E_{1z}\big|_{y=d/2} \\ E_{2z}\big|_{y=-d/2} = E_{3z}\big|_{y=-d/2} \\ H_{2x}\big|_{y=-d/2} = H_{3x}\big|_{y=-d/2} \end{cases}. \tag{A3}$$

Substituting equations A1 and A2 into A3 yields the following eigen equation:

$$\frac{\frac{k_1}{\varepsilon_1}\left[\frac{k_3}{\varepsilon_3}\left(1-e^{2k_2 d}\right)-\frac{k_2}{\varepsilon_2}\left(1+e^{2k_2 d}\right)\right]}{\frac{k_2}{\varepsilon_2}\left[\frac{k_3}{\varepsilon_3}\left(1+e^{2k_2 d}\right)-\frac{k_2}{\varepsilon_2}\left(1-e^{2k_2 d}\right)\right]} = 1+\frac{k_1}{\varepsilon_1}\frac{i\sigma_g}{\omega\varepsilon_0}. \tag{A4}$$

The q obtained by taking ε_2 in equation A4 as ε_{21} or ε_{22} represents the effective propagating wave-vector of the AGPPs in regions I or II, denoted as q_1 or q_2, respectively.

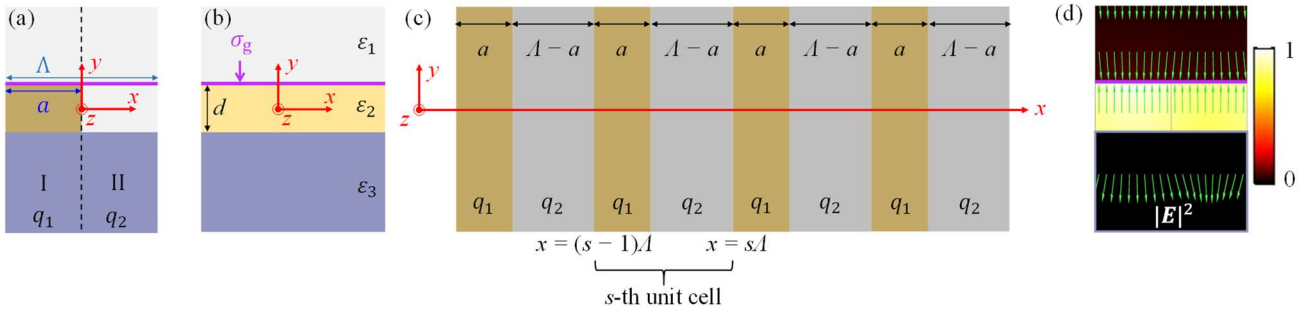

Figure S1. Cross-sections of the enlarged unit cell structure of the GIWAL (a), the three-medium slab waveguide with a surface conductivity (b), and the periodic two-medium slab waveguide (c), respectively. (d) The normalized electric field $|\boldsymbol{E}|^2$ of the AGPP modes on the cross-section of a unit cell of the GIWAL. Green arrows represent the polarization direction of the electric field of the AGPPs.

Now, the regions I and II could be regarded as homogeneous media of widths a and $\Lambda - a$, respectively, characterized by the effective wave-vectors q_1 and q_2, respectively. Furthermore, the TM guided mode mentioned above becomes the transverse electric (TE) mode propagating along the z-direction for this "new" structure since its electric field component lies mainly on the y-axis. Because the effective refractive index between adjacent unit cells of the GIWAL does not differ much, the GIWAL can be considered locally periodic. Thus, one unit cell in the GIWAL corresponds to one period in a periodic two-medium slab waveguide.[47]

The cross-section of the periodic two-medium slab waveguide is shown in Figure S1c. In the

waveguide, the electric field component of the TE wave propagating along the *z*-direction lies on the *y*-axis. The electric field in the *s*-th unit cell can be expressed as:

$$E_y(x,y,z,t)=\begin{cases}\{A_s e^{-ip_1[x-(s-1)\Lambda-a]}+B_s e^{ip_1[x-(s-1)\Lambda-a]}\}e^{-i(\omega t-k_z z)} & (s-1)\Lambda<x<(s-1)\Lambda+a\\ [C_s e^{-ip_2(x-s\Lambda)}+D_s e^{ip_2(x-s\Lambda)}]e^{-i(\omega t-k_z z)} & (s-1)\Lambda+a<x<s\Lambda\end{cases}, \quad \text{(A5)}$$

where $p_m^2 = q_m^2 - k_z^2$ (m = 1 or 2). $k_z = k_{zr} + ik_{zi}$ is the propagation constant of the AGPPs along the *z*-direction in a unit cell of the GIWAL. A_s, B_s, C_s, and D_s are undetermined mode coefficients, linked by boundary conditions.

According to Maxwell's equations and the expression of E_y, the magnetic field component of the TE wave along the *z*-axis in the *s*-th unit cell can be further solved as:

$$H_z(x,y,z,t)=\begin{cases}-\dfrac{p_1}{\omega\mu_0}\{A_s e^{-ip_1[x-(s-1)\Lambda-a]}-B_s e^{ip_1[x-(s-1)\Lambda-a]}\}e^{-i(\omega t-k_z z)} & (s-1)\Lambda<x<(s-1)\Lambda+a\\ -\dfrac{p_2}{\omega\mu_0}[C_s e^{-ip_2(x-s\Lambda)}-D_s e^{ip_2(x-s\Lambda)}]e^{-i(\omega t-k_z z)} & (s-1)\Lambda+a<x<s\Lambda\end{cases}, \quad \text{(A6)}$$

where μ_0 is the permeability in vacuum. Since E_y and H_z are continuous at the boundaries $x = (s-1)\Lambda$ and $(s-1)\Lambda + a$, we get:

$$\begin{cases}A_s e^{ip_1 a}+B_s e^{-ip_1 a}=C_{s-1}+D_{s-1}\\ p_1(A_s e^{ip_1 a}-B_s e^{-ip_1 a})=p_2(C_{s-1}-D_{s-1})\\ A_s+B_s=C_s e^{ip_2(\Lambda-a)}+D_s e^{-ip_2(\Lambda-a)}\\ p_1(A_s-B_s)=p_2[C_s e^{ip_2(\Lambda-a)}-D_s e^{-ip_2(\Lambda-a)}]\end{cases}. \quad \text{(A7)}$$

In addition, the periodic two-medium slab waveguide is similar to a one-dimensional crystal extending along the *x*-direction, and the periodicity conditions for the supported Bloch waves are:[47]

$$\begin{cases}C_s=e^{ik_x\Lambda}C_{s-1}\\ D_s=e^{ik_x\Lambda}D_{s-1}\end{cases}, \quad \text{(A8)}$$

where k_x represents the Bloch wavenumber along the *x*-direction, which depends on the incident angle of light. Substituting equation A8 into A7 derives the dispersion equation of the AGPPs propagating along the *z*-axis in the whole unit cell as:

$$\cos(k_x\Lambda)=\cos(p_1 a)\cos[p_2(\Lambda-a)]-\frac{1}{2}\left(\frac{p_2}{p_1}+\frac{p_1}{p_2}\right)\sin(p_1 a)\sin[p_2(\Lambda-a)]. \quad \text{(A9)}$$

The incident light is coupled into the GIWAL along the *z*-axis, so the Bloch wavenumber along the *x*-direction k_x is zero. k_z can be calculated quantificationally by solving equations A4 and A9 step by step. Then, the effective refractive index and the propagation length of the AGPPs in a unit cell are

defined as $n_{\mathrm{eff}} = k_{\mathrm{zr}}/k_0$ and $L = 1/(2k_{\mathrm{zi}})$, respectively.

As a visual guide, the electric field distribution of the AGPPs on the cross-section of a unit cell of the GIWAL is shown in Figure S1d. Consistent with the discussion in the manuscript, the AGPP modes have high field confinement, and almost all electromagnetic energy is confined at the dielectric grating between the graphene and metallic substrate. The polarization direction of the electric field represented by the green arrow in Figure S1d indicates that the electric field of the AGPP modes mainly lies on the y-axis.

Section 2: The effect of different parameters on the trend of n_{eff} versus a

The increased relaxation rate of graphene results in a greater loss and thus a smaller propagation length of the AGPPs, but does not affect n_{eff}, as shown in Figures S2a and S2b. Furthermore, decreasing the chemical potential of graphene or the thickness of the dielectric grating leads to a larger n_{eff}, as shown in Figures S2c and S2d, but the trend of n_{eff} versus a is independent of the chemical potential of graphene and the thickness of the dielectric grating, as shown by normalized n_{eff} in Figures S2c and S2d. This property means that changes in the chemical potential of graphene and the thickness of the dielectric grating do not affect the focus of the on-chip focusing of the AGPPs in the GIWAL.

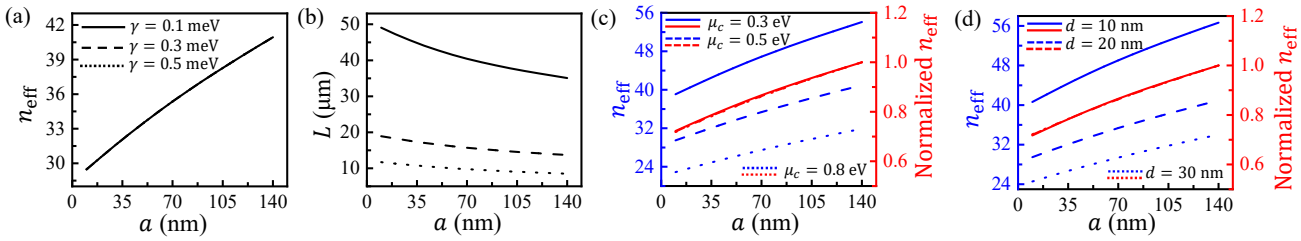

Figure S2. Dependences of the effective refractive index (a) and the propagation length (b) of the AGPPs on the width of the dielectric strip for different relaxation rates of graphene. Dependences of the effective refractive index of the AGPPs on the width of the dielectric strip for different chemical potentials of graphene (c) and different thicknesses of the dielectric grating (d), respectively. The frequency of the incident light is f = 15 THz.

As shown in Figure S3, as the relative permittivity or the period of the dielectric grating increases, the wavelength-independent trend of n_{eff} versus a is broken negligibly.

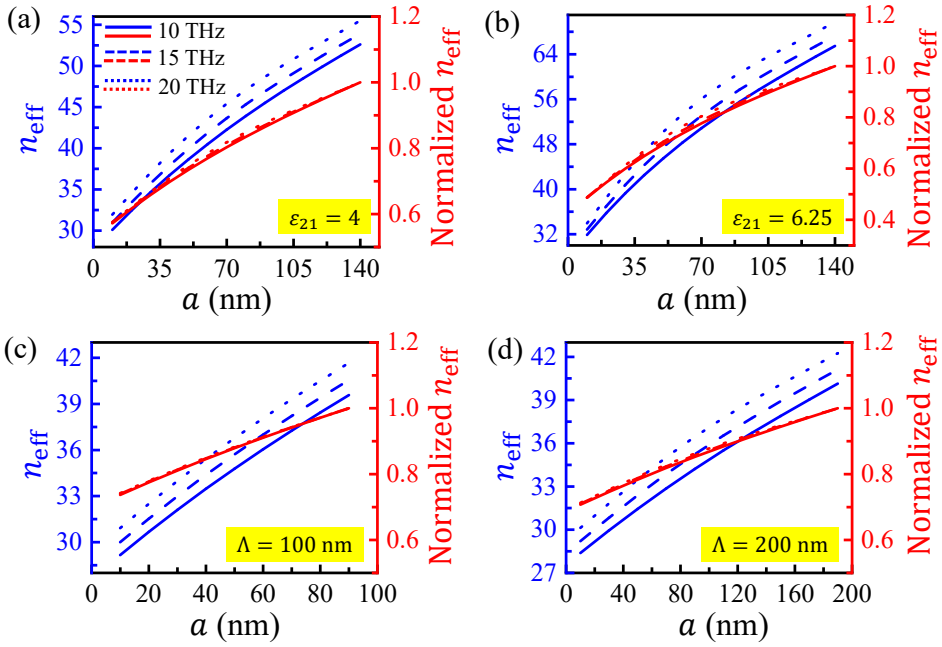

Figure S3. Dependences of the effective refractive index of the AGPPs on the width of the dielectric strip for different frequencies of the incident light under $\varepsilon_{21} = 4$ (a), $\varepsilon_{21} = 6.25$ (b), $\Lambda = 100$ nm (c), and $\Lambda = 200$ nm (d), respectively.

Section 3: Coupling the incident light to the AGPP modes

We use a coupling grating to couple the incident light to the AGPP modes, which then propagate through the GIWAL along the z-direction and achieve on-chip focusing in the GIWAL, as shown in Figure S4a. We analyze the coupling details quantitatively here.

The propagation constant p_c of the AGPPs supported by the coupling grating and propagating along the z-direction can be calculated from equation A4:

$$\frac{\frac{k_1}{\varepsilon_1}\left[\frac{k_3}{\varepsilon_3}\left(1-e^{2k_2d}\right)-\frac{k_2}{\varepsilon_2}\left(1+e^{2k_2d}\right)\right]}{\frac{k_2}{\varepsilon_2}\left[\frac{k_3}{\varepsilon_3}\left(1+e^{2k_2d}\right)-\frac{k_2}{\varepsilon_2}\left(1-e^{2k_2d}\right)\right]}=1+\frac{k_1}{\varepsilon_1}\frac{i\sigma_g}{\omega\varepsilon_0}, \quad \text{(C1)}$$

where $k_j^2 = p_c^2 - \varepsilon_j k_0^2$ (j = 1, 2, or 3). For the AGPPs propagating along the z-direction, the relative permittivity of the dielectric grating in the coupling grating can be equivalent to $\varepsilon_2 = f_c\varepsilon_{21} + (1 - f_c)\varepsilon_{22}$,[51] where $f_c = w_c/\Lambda_c$ is the filling factor, and w_c and Λ_c are the width of the dielectric strip and the period of the dielectric grating in the coupling grating, respectively. Here, we consider f_c as 0.5.

In addition, the coupling grating can diffract the incident light that strikes perpendicular to the graphene surface along the y-direction. The wave-vector of the m-th order diffracted light in the z-direction is $k_{zc,\,m} = 2m\pi/\Lambda_c$ (m = 1, 2, 3, …). We only consider the first order diffracted light here, i.e., m = 1. When the phase matching condition $\mathrm{Re}(p_c) = 2\pi/\Lambda_c$ is satisfied, the incident light can be efficiently coupled to the AGPP mode.

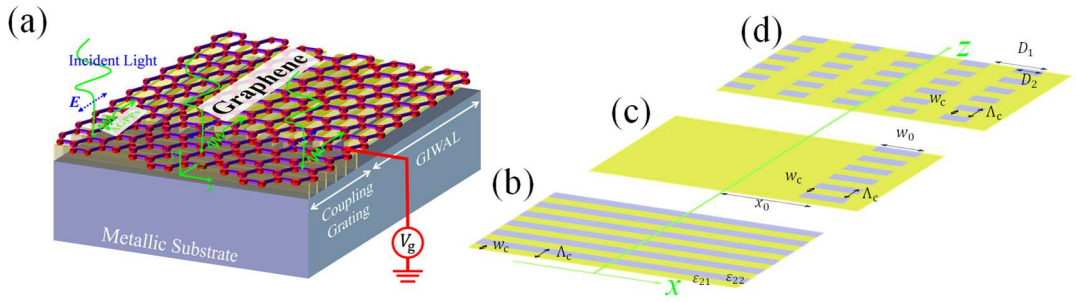

Figure S4. (a) Schematic representation of coupling the incident light to the AGPP mode. (b-d) Top views of the dielectric grating in the coupling grating on the y = 0 plane for the extended grating (b), the local grating (c), and the digitally encoded grating (d), respectively.

(1) Numerical simulations of Figure 2e and the middle panel of Figure 3a in the main manuscript adopt the coupling grating of Figure S4b. The frequency of the incident light is f =15 THz, and the chemical potential of graphene is μ_c = 0.5 eV. $\mathrm{Re}(p_c) = 1.12 \times 10^7$ m^{-1} from equation C1, so Λ_c is designed to be 561 nm.

(2) Numerical simulations of the lower panel of Figure 3a in the main manuscript adopt the coupling grating of Figure S4b. The frequency of the incident light is f =10 THz. $\mathrm{Re}(p_c) = 1.12 \times 10^7$ m^{-1} is required to maintain the structure of the coupling grating, so the chemical potential of graphene needs to be electrically tuned to 0.22 eV according to equation C1.

(3) Numerical simulations of the upper panel of Figure 3a in the main manuscript adopt the coupling grating of Figure S4b. The frequency of the incident light is f =20 THz. $\mathrm{Re}(p_c) = 1.12 \times 10^7$ m^{-1} is required to maintain the structure of the coupling grating, so the chemical potential of graphene needs to be electrically tuned to 0.89 eV according to equation C1.

(4) Numerical simulations of Figure 2f in the main manuscript adopt the coupling grating of Figure S4c. The frequency of the incident light is f =15 THz, and the chemical potential of graphene is μ_c = 0.5 eV. $\mathrm{Re}(p_c) = 1.12 \times 10^7$ m^{-1} from equation C1, so Λ_c is designed to be 561 nm. In addition, x_0 and w_0 are 3 μm and 1.5 μm respectively.

(5) Numerical simulations of Figure 4c in the main manuscript adopt the coupling grating of Figure S4d. The frequency of the incident light is f =15 THz, and the chemical potential of graphene is μ_c = 0.5 eV. Re(p_c) = 1.12 × 10^7 m^{-1} from equation C1, so Λ_c is designed to be 561 nm. In addition, D_1 and D_2 are 1.8 μm and 0.9 μm respectively.

(6) Numerical simulations of Figure 4a in the main manuscript adopt the coupling grating of Figure S4d. The frequency of the incident light is f =10 THz. Re(p_c) = 1.12 × 10^7 m^{-1} is required to maintain the structure of the coupling grating, so the chemical potential of graphene needs to be electrically tuned to 0.22 eV according to equation C1. In addition, D_1 and D_2 are 1.8 μm and 0.45 μm respectively.

(7) Numerical simulations of Figure 4e in the main manuscript adopt the coupling grating of Figure S4d. The frequency of the incident light is f =20 THz. Re(p_c) = 1.12 × 10^7 m^{-1} is required to maintain the structure of the coupling grating, so the chemical potential of graphene needs to be electrically tuned to 0.89 eV according to equation C1. In addition, D_1 and D_2 are 1.8 μm and 1.35 μm respectively.

Next, we calculate the effect of the unit cell number (N) of the coupling grating on the coupling efficiency (η), defined as $\eta = P_{AGPP}/P_{in}$. Here, P_{in} and P_{AGPP} represent the power of the incident light and the power of the AGPP mode, respectively, as shown in Figure S5a. The coupling efficiency as a function of the unit cell number is shown in Figure S5b. The results show that the reduced number of unit cells leads to slightly decreased coupling efficiency for 20 < N <50.

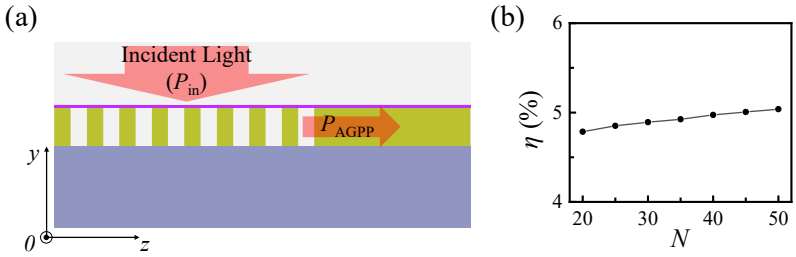

Figure S5. (a) Side view of the coupling grating with the GIWAL. (b) The coupling efficiency as a function of the unit cell number of the coupling grating. The frequency of the incident light is f = 20 THz.

Section 4: Hybridization between the AGPPs and phonons of the SiO_2 grating

In order to directly account for the hybridization between the AGPPs and phonons of the SiO_2

grating in the theoretical model proposed in Section 1 of the Supplementary information, the most straightforward manner is to replace the constant permittivity of the SiO_2 grating (ε_{21} = 2.25) with a generalized, frequency-dependent complex dielectric function $\varepsilon_{21}(\omega)$:[30]

$$\varepsilon_{21}(\omega) = \varepsilon_{\infty} + \sum_{j=1}^{3} s_j \frac{\omega_j^{\,2}}{\omega_j^{\,2} - \omega^2 - i\omega\Gamma_j}, \tag{D1}$$

where the high-frequency permittivity is ε_{∞} = 2.4, the frequency of j-th phonon is ω_j = {448.3, 792.2, 1128.8} cm^{-1}, the oscillator strength of j-th phonon is s_j = {0.7514, 0.1503, 0.6011}, and the scattering rate of j-th phonon is Γ_j = {26.7, 42.4, 42.4} cm^{-1}. Within the frequency band of interest, the SiO_2 exhibits a phonon resonance characterized by a Lorentz oscillation, as shown in Figure S6a.

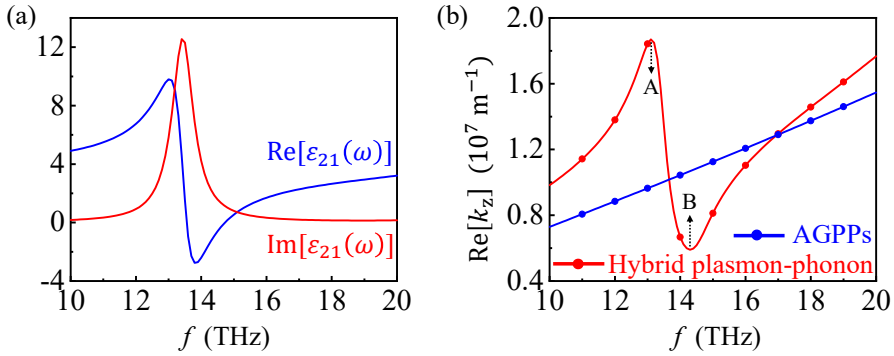

Figure S6. (a) Dependences of the real part (blue) and the imaginary part (red) of the complex dielectric function $\varepsilon_{21}(\omega)$ on the operating frequency. (b) Dependences of the real part of the propagation constant along the z-direction in a unit cell of the GIWAL on the operating frequency for the original pure AGPPs (blue, ε_{21} is 2.25) and the hybrid plasmon-phonon mode (red, ε_{21} is $\varepsilon_{21}(\omega)$). The solid lines and circles represent the analytical results and the numerical simulations, respectively, which are highly consistent.

By solving equations A4 and A9 step by step, for a unit cell of the GIWAL (with a = 75 nm), the dispersion curves of the original pure AGPPs and the hybrid plasmon-phonon mode are plotted in Figure S6b. When the operating frequency is far away from the phonon frequency (ω_1 = 448.3 cm^{-1} or f = 13.44 THz), the proportion of the AGPPs in the hybrid plasmon-phonon mode increases gradually, because the dispersion curve of the hybrid plasmon-phonon mode is close to that of the AGPPs. Conversely, when the operating frequency is close to the phonon frequency, the proportion of phonons in the hybrid plasmon-phonon mode increases gradually. Furthermore, since we obtain the complex propagation constant by inputting the real frequency into the equations A4 and A9, the hybrid plasmon-

phonon mode exhibits anomalous dispersion in the region from point A to point B. This manifestation accompanied by an anti-crossing behavior is the hallmark of the mode hybridization.

Section 5: Derivation of the trajectory equation of the light ray in Mikaelian lens

The fundamental equation used to deal with problems within the framework of geometrical optics is the ray equation:[37]

$$\frac{d}{ds}\left(n\frac{d\vec{r}}{ds}\right)=\nabla n\,. \tag{E1}$$

Its component form is:

$$\begin{cases}\dfrac{d}{ds}\left(n\dfrac{dx}{ds}\right)=\dfrac{\partial n}{\partial x}\\ \dfrac{d}{ds}\left(n\dfrac{dy}{ds}\right)=\dfrac{\partial n}{\partial y}\\ \dfrac{d}{ds}\left(n\dfrac{dz}{ds}\right)=\dfrac{\partial n}{\partial z}\end{cases}. \tag{E2}$$

Considering only the evolution of light on the $y = 0$ plane, and assuming that the refractive index n is only related to the x-coordinate, that is, $n = n(x)$, the equation E2 becomes:

$$\begin{cases}\dfrac{d}{ds}\left(n\dfrac{dx}{ds}\right)=\dfrac{dn}{dx}\\ \dfrac{d}{ds}\left(n\dfrac{dz}{ds}\right)=0\end{cases}. \tag{E3}$$

The formula for the z-coordinate in equation E3 is:

$$n\frac{dz}{ds}=c_1\,, \tag{E4}$$

where the integration constant c_1 is related to the incident point and the incident angle of light. For a ray of normal incidence at $x = x_0$, c_1 can be characterized by the refractive index at x_0, i.e., $c_1 = n(x_0)$. Considering $(ds)^2 = (dx)^2 + (dz)^2$, equation E4 is further written as:

$$dz=\frac{c_1}{\sqrt{n^2-c_1^{\,2}}}dx\,. \tag{E5}$$

We are concerned with Mikaelian lens of the refraction index $n(x) = n_0\mathrm{sech}(\xi x)$, so equation E5 becomes:

$$dz = \frac{\cosh(\xi x)}{\sqrt{\sinh^2(\xi x_0) - \sinh^2(\xi x)}} dx. \tag{E6}$$

Direct integration of equation E6 yields:

$$\tan(\xi z + c_2) = \frac{\sinh(\xi x)}{\sqrt{\sinh^2(\xi x_0) - \sinh^2(\xi x)}}, \tag{E7}$$

where the integration constant c_2 can then be determined by the incident point. Since

$$\tan(\xi z + c_2) = \frac{\sin(\xi z + c_2)}{\sqrt{1 - \sin^2(\xi z + c_2)}}, \tag{E8}$$

equation E7 translates to:

$$\sinh(\xi x) = \sin(\xi z + c_2)\sinh(\xi x_0). \tag{E9}$$

Substituting the incident point of the ray, $(x, z) = (x_0, 0)$, into equation E9 determines c_2 to be $\pi/2$. So the trajectory equation of the light ray on the $y = 0$ plane in Mikaelian lens is:

$$x(z) = \frac{1}{\xi}\sinh^{-1}\left[\sin\left(\xi z + \frac{\pi}{2}\right)\sinh(\xi x_0)\right]. \tag{E10}$$

Section 6: The complete structure of the GIWAL with 61 unit cells

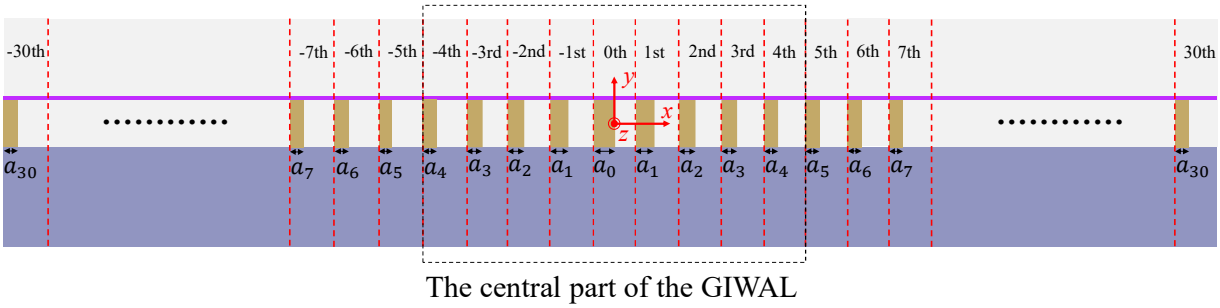

Figure S7. The cross-section of the complete structure of the GIWAL with 61 unit cells. In order to make the unit cell details clearer, we only show the central part of the GIWAL in Figures 1a and 1b of the manuscript, as shown by the area enclosed by the black dotted box. To achieve achromatic on-chip focusing of the AGPPs, the refractive index profile of the GIWAL needs to be symmetric, so the -*i*-th cell needs to be the same as the *i*-th cell (correspondingly, the width of their dielectric strips is the same).

Section 7: Comparison for the precise and stepped GIWALs under different unit cell numbers

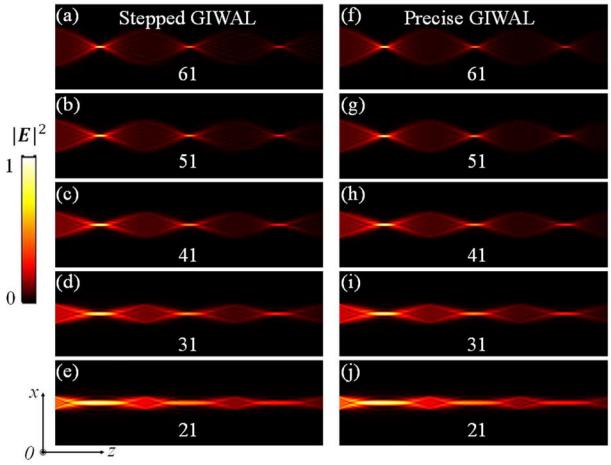

Figure S8. The normalized electric field $|\boldsymbol{E}|^2$ of the AGPPs traveling along the z-axis on the $y = 0$ plane in the stepped (a-e) and precise (f-j) GIWALs for the unit cell number of 61 (a, f), 51 (b, g), 41 (c, h), 31 (d, i), and 21 (e, j), respectively. The frequency of the incident light is $f = 15$ THz and the focal length of the on-chip focusing is $f_L = 10$ μm. It is worth noting that different unit cell numbers have no essential effect on the propagation distance of the AGPP mode. However, an increase in the number of unit cells results in a smaller focal depth and focal point and higher focusing efficiency. In addition, when the number of unit cells increases to 61, the focusing performance remains basically unchanged, so we use 61 unit cells here.

Section 8: Effects of inherent losses of the AGPPs

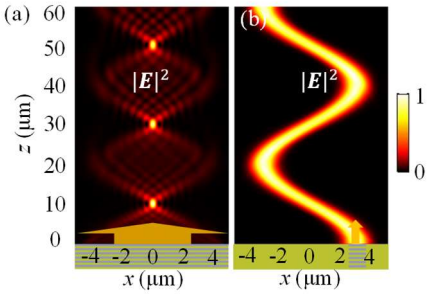

Figure S9. The normalized electric field $|\boldsymbol{E}|^2$ of the AGPPs traveling along the z-axis on the $y = 0$ plane in the stepped GIWAL for the incident light coupled with an extended grating (a) or a local grating (b). These numerical simulations do not include the inherent losses of the AGPPs. The frequency of the incident light is $f = 15$ THz and the focal length of the on-chip focusing is $f_L = 10$ μm.

Section 9: Propagation properties of TE modes supported by graded index waveguides

Figure S10a shows the cross-section of the waveguide with a graded refractive index of $n(x) = n_0\text{sech}(\xi x)$. The electric field of TE modes traveling along the z-direction lies on the y-axis and can be written as:

$$E_Y\left(x,y,z,t\right) = E_y(x)e^{-i(\omega t-\beta z)}. \tag{I1}$$

Substituting equation I1 into Maxwell's equations, the wave equation satisfied by $E_y(x)$ can be solved as:

$$\frac{d^2E_y(x)}{dx^2}+\left[k_0{}^2n^2(x)-\beta^2\right]E_y(x)=0. \tag{I2}$$

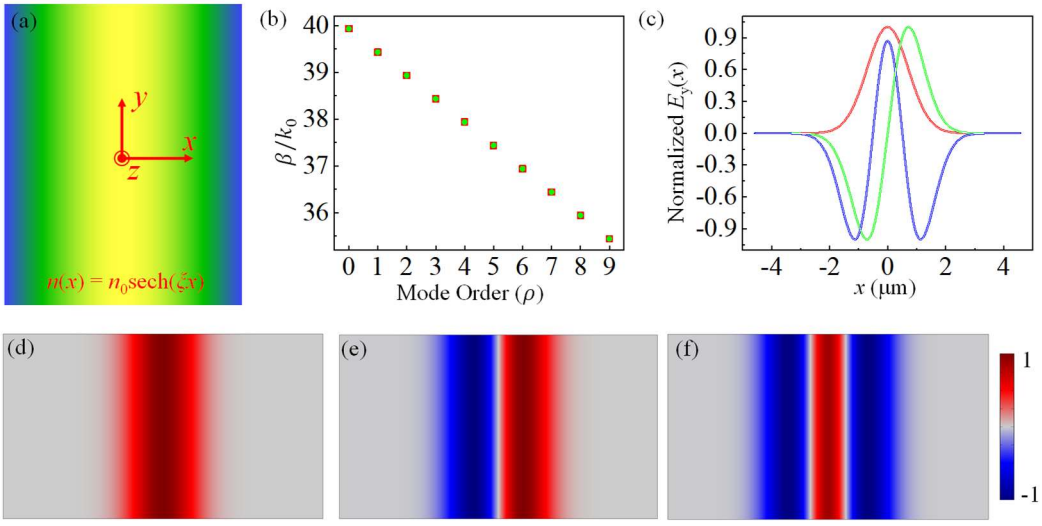

Figure S10. (a) The cross-section of the waveguide with a graded refractive index of $n(x) = n_0\text{sech}(\xi x)$. (b) Propagation constants from equation I9 (red squares) and numerical simulations (green circles), respectively. (c) The normalized electric field $E_y(x)$ on the x-axis for the 0th (red), 1st (green), and 2nd (blue) order waveguide modes. The white curve on the corresponding curve is the result of the numerical simulation. (d-f) The normalized electric field $E_y(x)$ on the cross-section of the waveguide for the 0th (d), 1st (e), and 2nd (f) order waveguide modes. n_0 = 40.186, $\xi = \pi/20$ μm^{-1}, and the frequency of the incident light is f = 15 THz.

Substitute $n(x) = n_0\text{sech}(\xi x)$ into equation I2 and let

$$E_y(x) = W(x)\text{sech}^s(\xi x), \tag{I3}$$

where s is an undetermined constant and its function is to make the equation satisfied by $W(x)$ have the most concise form, then equation I2 can be transformed into:

$$\frac{d^2W(x)}{dx^2}-2s\xi\tanh(\xi x)\frac{dW(x)}{dx}+\left[\xi^2\left(s^2+s-\frac{{k_0}^2{n_0}^2}{\xi^2}\right)\tanh^2(\xi x)+\xi^2\left(\frac{{k_0}^2{n_0}^2}{\xi^2}-s\right)-\beta^2\right]W(x) \quad \text{(I4)}$$
$$=0.$$

In order to make equation I4 have the most concise form, we can set $s^2 + s - {k_0}^2{n_0}^2/\xi^2 = 0$, that is,

$$s=\frac{\sqrt{1+\frac{4{k_0}^2{n_0}^2}{\xi^2}}-1}{2}. \quad \text{(I5)}$$

Therefore, equation I4 simplifies to:

$$\frac{d^2W(x)}{dx^2}-2s\xi\tanh(\xi x)\frac{dW(x)}{dx}+\left[\xi^2s^2-\beta^2\right]W(x)=0. \quad \text{(I6)}$$

Now, introducing the variable

$$\zeta=-\sinh^2(\xi x), \quad \text{(I7)}$$

the equation I6 can be transformed into:

$$\zeta(1-\zeta)\frac{d^2W(\zeta)}{d\zeta^2}+\left[S_3-(S_1+S_2+1)\zeta\right]\frac{dW(\zeta)}{d\zeta}-S_1S_2W(\zeta)=0, \quad \text{(I8)}$$

where $S_1 = (\rho - 2s)/2$, $S_2 = -\rho/2$, $S_3 = 1/2$, and $(s - \rho)^2 = \beta^2/\xi^2$, that is,

$$\beta=\sqrt{{k_0}^2{n_0}^2+\frac{1}{4}\xi^2}-\left(\rho+\frac{1}{2}\right)\xi, \quad \text{(I9)}$$

of which $\rho = 0, 1, 2, \ldots$ is the mode order. Equation I8 is the standard form of Gaussian hypergeometric differential equation whose solution is Gaussian hypergeometric function:

$$W(\zeta)=\begin{cases}{}_2\mathrm{F}_1(S_1,S_2,S_3,\zeta) \text{ for } \rho=0,2,4,...\\ {}_2\mathrm{F}_1(S_1-S_3+1,S_2-S_3+1,2-S_3,\zeta)\zeta^{1-S_3} \text{ for } \rho=1,3,5,...\end{cases}. \quad \text{(I10)}$$

Now, combining equations I3, I7, and I10, the normalized electric field $E_y(x)$ can be obtained as:

$$E_y(x)=AQ(x), \quad \text{(I11)}$$

where

$$Q(x)=\begin{cases}{}_2\mathrm{F}_1\left[S_1,S_2,S_3,-\sinh^2(\xi x)\right]\mathrm{sech}^s(\xi x) \text{ for } \rho=0,2,4,...\\ {}_2\mathrm{F}_1\left[S_1-S_3+1,S_2-S_3+1,2-S_3,-\sinh^2(\xi x)\right]\sinh(\xi x)\,\mathrm{sech}^s(\xi x) \text{ for } \rho=1,3,5,...\end{cases}, \quad \text{(I12)}$$

and the normalization constant A is calculated by using

$$\int_{-\infty}^{\infty}\left|E_y(x)\right|^2dx=A^2\int_{-\infty}^{\infty}\left|Q(x)\right|^2dx=1, \quad \text{(I13)}$$

that is:

$$A = \left(\frac{1}{\int_{-\infty}^{\infty} |Q(x)|^2 \, dx} \right)^{1/2} . \tag{I14}$$

Figure S10b presents the propagation constants from equation I9 and numerical simulations, which are in good agreement. Figure S10c presents the normalized electric field from equation I11 and the numerical simulation, which is also highly consistent. Figures S10d-S10f present the normalized electric field distributions of the first three-order TE modes on the cross-section.

Section 10: The distributions of $|E|^2$ on the line of $y = 0$

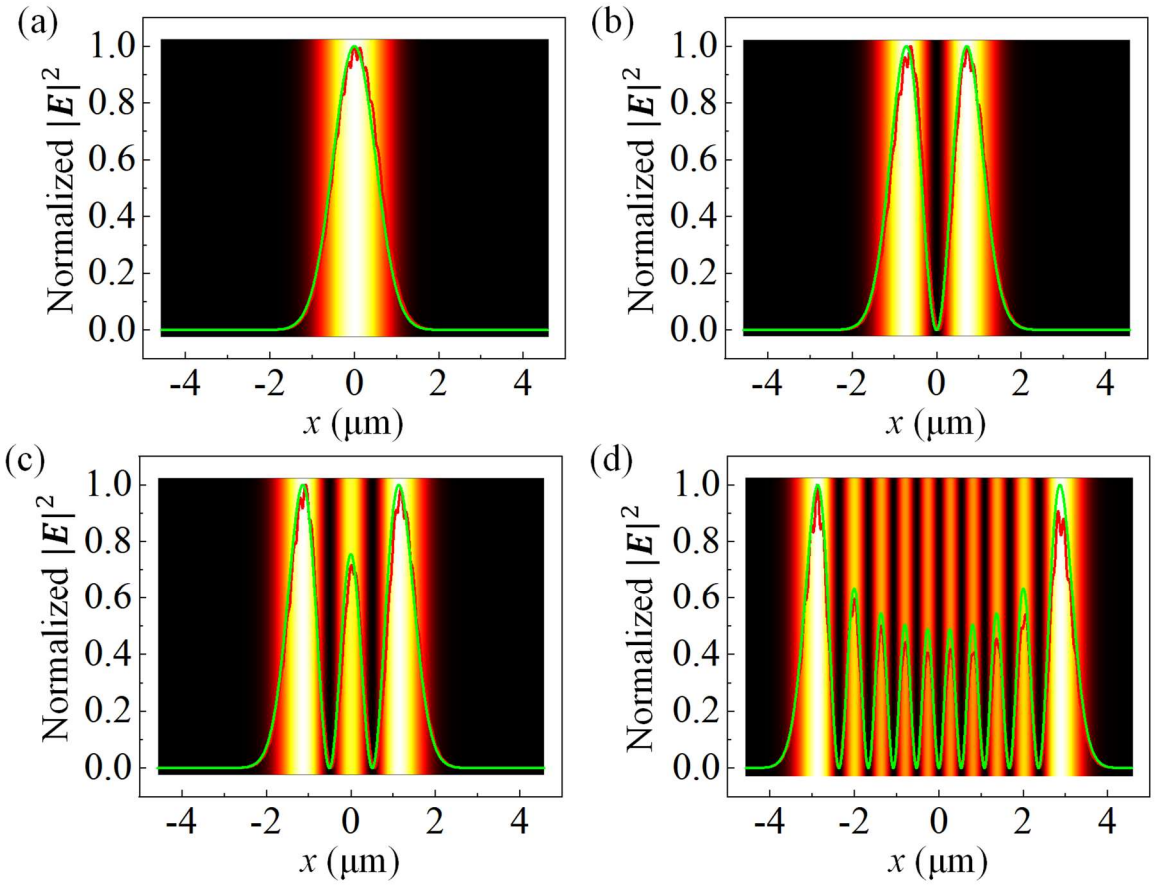

Figure S11. The distributions of the normalized electric field $|E|^2$ on the line of $y = 0$ for the 0th (a), 1st (b), 2nd (c), and 9th (d) order waveguide modes. The red and green curves correspond to the simulated stepped GIWAL and the theoretical Mikaelian lens, respectively. The background picture represents the normalized electric field $|E|^2$ of the Mikaelian lens on the cross-section.

Section 11: Beam evolution in the waveguide

We only need to study the component of the electric field along the y-axis on the $y = 0$ plane in the waveguide. All eigenmodes $E_{y\rho}(x, z)$ supported by the waveguide are orthonormal, i.e.,

$$\int_{-\infty}^{\infty} E_{y\rho'}^{*}(x,z) \times E_{y\rho}(x,z)dx = \delta_{\rho\rho'} = \begin{cases} 0 & (\rho \neq \rho') \\ 1 & (\rho = \rho') \end{cases}, \tag{K1}$$

so they can be treated as basic unit vectors to build a generalized coordinate system. Thus, in this generalized coordinate system, an arbitrary field distribution $E_y(x, z)$ in the waveguide can be expressed as a linear superposition of these eigenmodes:

$$E_y(x,z) = \sum_{\rho=0}^{\infty} c_\rho E_{y\rho}(x,z), \tag{K2}$$

where c_ρ is the expansion coefficient of the ρ-th order eigenmode, and the solution process is as follows.

According to equation K2, the initial incident field $E_y(x, 0)$ at $z = 0$ in this waveguide can be expanded as:

$$E_y(x,0) = \sum_{\rho=0}^{\infty} c_\rho E_{y\rho}(x,0). \tag{K3}$$

Perform further math on equation K3:

$$\begin{aligned} \int_{-\infty}^{\infty} E_{y\rho'}^{*}(x,0) \times E_y(x,0)dx &= \int_{-\infty}^{\infty} E_{y\rho'}^{*}(x,0) \times \left[\sum_{\rho=0}^{\infty} c_\rho E_{y\rho}(x,0) \right] dx \\ &= \sum_{\rho=0}^{\infty} c_\rho \int_{-\infty}^{\infty} E_{y\rho'}^{*}(x,0) \times E_{y\rho}(x,0)dx \\ &= \sum_{\rho=0}^{\infty} c_\rho \delta_{\rho\rho'} = c_{\rho'}. \end{aligned} \tag{K4}$$

Replacing the subscript ρ' in equation K4 with ρ, we get:

$$c_\rho = \int_{-\infty}^{\infty} E_y(x,0) E_{y\rho}^{*}(x,0)\, dx. \tag{K5}$$

These analyses show that the field distribution in the waveguide depends on both the eigenmodes $E_{y\rho}(x, z)$ and the initial incident field $E_y(x, 0)$. It can therefore be concluded that the field distribution in the waveguide originates from the evolution of the incident field.

Section 12: Self-focusing and self-collimation of Gaussian beams in the GIWAL

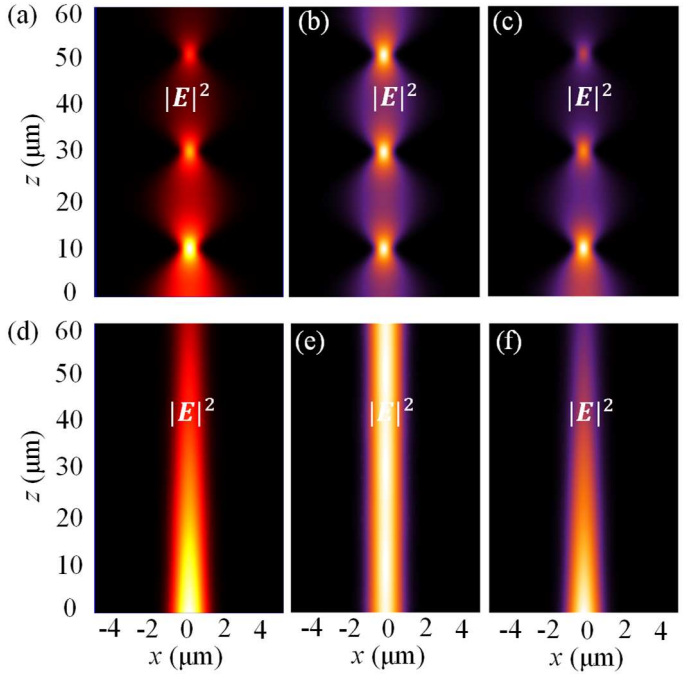

Figure S12. The normalized electric field $|\boldsymbol{E}|^2$ of the AGPPs traveling along the z-axis on the $y = 0$ plane for the Gaussian beam of $x_0 = 0$ μm and $w_0 = 3$ μm (a-c) and $x_0 = 0$ μm and $w_0 = 1.45$ μm (d-f). (a-c) and (d-f) reveal the self-focusing and self-collimation of the Gaussian beam, respectively. (a, d), (b, e), and (c, f) represent numerical simulations with losses, analytical results without losses, and analytical results with losses, respectively. The frequency of the incident light is $f = 15$ THz and the focal length of the on-chip focusing is $f_L = 10$ μm.

Section 13: Analytical prediction for the spatial inverter based on the achromatic GIWAL

The electric field $E_y(x, 0)$ of the incident digital optical signal is:

$$E_y(x,0)=\begin{cases}1, & -\dfrac{D_1}{2}+\alpha D_1 < x < -\dfrac{D_1}{2}+\alpha D_1+D_2 \\ 0, & \text{else}\end{cases}, \tag{M1}$$

where D_1 and D_2 are the oscillation period of the digital optical signal and the width with an intensity of 1, respectively. $\alpha = -2, -1, 0, 1$, and 2. Simultaneous equation M1 and equations 2-7 in the main manuscript can obtain the evolution of the digital optical signal on the $y = 0$ plane in the GIWAL, as shown in Figure S13.

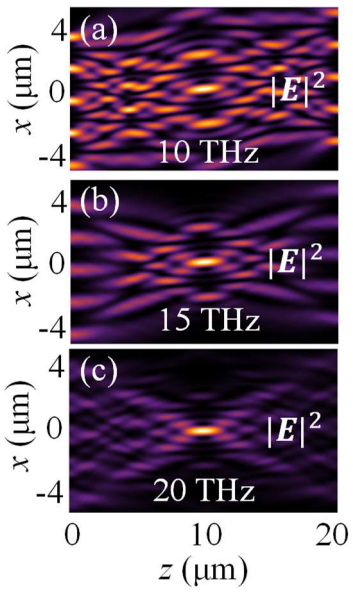

Figure S13. The normalized electric field $|\boldsymbol{E}|^2$ of the AGPPs propagating along the z-direction on the $y = 0$ plane in the GIWAL for incident frequencies of 10 THz (a, D_1 = 1.8 μm and D_2 = 0.45 μm), 15 THz (b, D_1 = 1.8 μm and D_2 = 0.9 μm), and 20 THz (c, D_1 = 1.8 μm and D_2 = 1.35 μm), respectively.